

An activity rate model of induced seismicity
within the Groningen Field

S.J.Bourne, S.J. Oates

30 September, 2014

CONFIDENTIAL DRAFT

Abstract

Gas production from the Groningen Field located in the north of the Netherlands induces earthquakes of sufficient number and magnitude to cause concern about the level of seismic risk. An essential part of assessing this risk is a probabilistic seismological model to forecast the future probabilities of earthquakes induced under future gas production plans. Here we present an alternative seismological model that provides a more precise description of the relationship between observed seismicity and reservoir compaction.

This has been achieved using a Poisson Point Process model to describe the nucleation rate of earthquakes in response to reservoir compaction and the Epidemic Type Aftershock Sequence model to describe the triggering of additional events. Joint maximum likelihood parameter estimates were obtained and Monte Carlo analysis was used to quantify uncertainties in these estimates. Simulations of seismicity using these parameter estimates are in good agreement with all aspects of past seismicity.

The model achieves more reliable parameter estimates and more precise forecasts than the existing Strain Partitioning model. Furthermore, it provides a complete description of aftershocks that critically influence the year-to-year variability in seismicity and therefore must be properly included in the Probabilistic Seismic Risk Analysis. This activity rate model provides the most complete framework yet for forecasting future seismicity under different plans for future gas production.

1 Introduction

Gas production from the Groningen Field induces seismicity that in recent years has started to cause concerns about the future strength of earthquake ground motions and the resilience of existing buildings to these ground motions. Ongoing gas production is depleting the pressure of hydrocarbon gas within the reservoir pore space causing the reservoir to compact. In turn, reservoir compaction increases the mechanical loads acting on pre-existing geological faults within and close to the reservoir. Some small fraction of these faults become unstable and are therefore prone to slip. Abrupt slip on such a fault results in an earthquake that radiates seismic energy.

The established method for assessing the future likelihood of ground motion events is Probabilistic Seismic Hazard Assessment (PSHA) (*e.g.* Cornell,

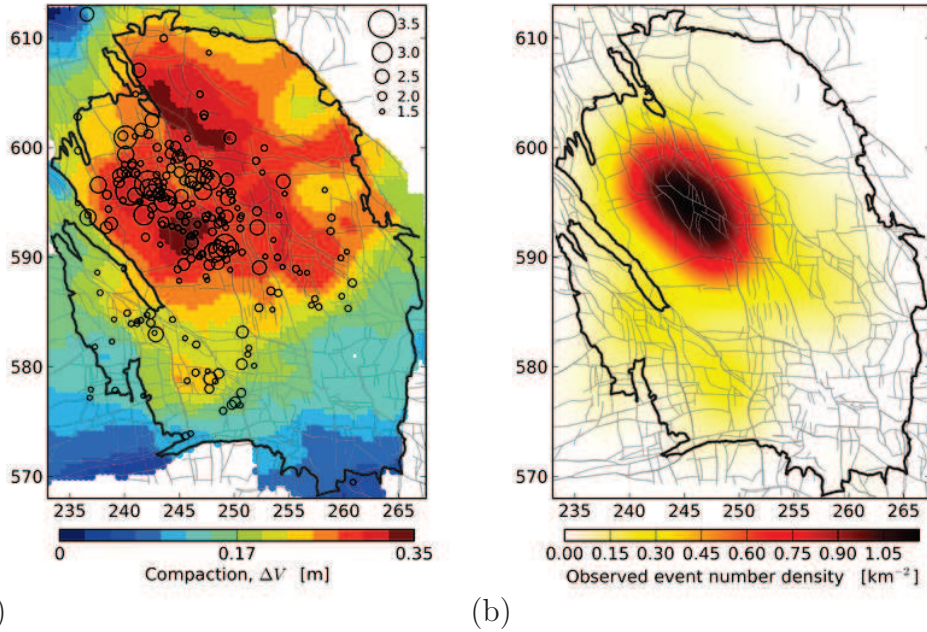


Figure 1: (a) Location map of earthquakes in relation to the field boundary, faults mapped at the top Rotliegendes and reservoir compaction up to 2013 according to the time-decay compaction model. Circle area denotes the magnitude as indicated by the legend. Map coordinates are given as kilometres within the Dutch National coordinate system (Rijksdriehoek). (b) The probability density function of epicentres estimated from the $M \geq 1.5$ events observed between April 1995 and August 2014 using the method of Gaussian kernels. The kernel bandwidth was estimated according Scott's rule (Scott, 1992) and the results are expressed as an event number density.

1968; McGuire, 2008). The two essential elements of PSHA are a seismological model to describe the probability distribution of possible future earthquake locations and magnitudes, and a ground motion model to describe the probability distribution of ground motions, such as peak ground accelerations, at a given distance from an earthquake of a given magnitude. The convolution of these two elements yields an estimate for the probability distribution of future ground motion events at a site of interest. Likewise, the established method for assessing the future likelihood of building damage or injury due to earthquake ground motions is Probabilistic Seismic Risk Assessment (PSRA). This is an extension of PSHA that further convolves the seismic hazard models with the probability of building damage for a given ground motion event and the probability of injury for a given building damage event.

PSHA and PSRA for the Groningen Field both require a reliable, site-specific, model for seismicity induced by reservoir compaction. There is fundamental physical reason to look for a relationship between induced seismicity and induced strain. An earthquake constitutes an increment of slip of one side of a fault surface relative to the other. This discontinuity in displacement across the fault surface represents an increment of strain. This is measured by the seismic moment of the event defined as

$$M_o = \mu DS, \quad (1)$$

where D is the average slip on the fault, S is the area of the fault slip, and μ is

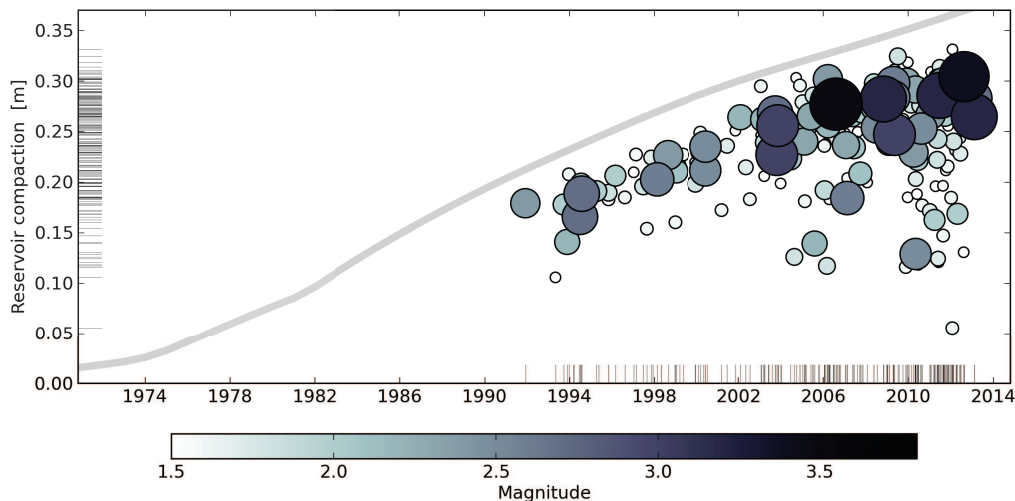


Figure 2: Time series of $M \geq 1.5$ earthquake magnitudes versus reservoir compaction at the origin time and epicentre of each event.

the shear modulus of the surrounding medium. Consequently, a population of earthquakes within some spatial volume and time interval represent an average incremental strain due to seismic slip on faults (seismic strain) as described by Kostrov (1974)

$$\bar{\epsilon}_{ij} = \frac{1}{2\mu V} \sum_{k=1}^N M_o^k m_{ij}^k \quad (2)$$

where N is the number of events within the volume, V is the volume, M_o^k and m_{ij}^k are the seismic moment and unit moment tensor of the k^{th} event respectively.

Similarly, geodetic measurements of surface displacements provide a measure of the induced strain due to gas production in the form reservoir compaction. Clearly, there must be a relationship induced strain and induced earthquakes. In the extreme case that all induced strain is accommodated by earthquakes the geodetic strain and seismic strains must be equal. Otherwise seismic strains must be smaller than the induced strains. In this case, other mechanisms accommodate the induced strain such as elastic and aseismic plastic deformations. The former stores elastic energy which remains available for release by future earthquakes, the latter dissipates energy without any associated seismicity. The presence of pre-existing faults and other geological heterogeneities means the relative contribution of seismic strain to the total induced strain may vary from place to place. However, these possible effects may not be visible if the controlling heterogeneities are sufficiently small-scale and densely distributed.

Motivated by these physical considerations about induced earthquakes conforming in some manner to the induced strain field we start by investigating the relationship between induced seismicity and reservoir compaction. To that end we note that the distribution of observed earthquake epicentres conforms to the areal distribution of reservoir compaction inferred from the observed distribution of surface subsidence (Figure 1). Likewise the observed temporal distribution of earthquakes conforms to the development of reservoir compaction through time (Figure 2) in the sense that earthquakes exhibit a sustained preference for regions of higher compaction through time. This suggests nucleation of earthquakes depends on compaction, but does not suggest a casual link between compaction and magnitude. If magnitudes are independent of compaction, the larger magnitudes are still more likely to occur in regions where there are more events. The relationship with mapped faults is however rather uncertain at present because the random measurement errors in epicentral locations are large relative to typical distances between mapped faults (Figure 3).

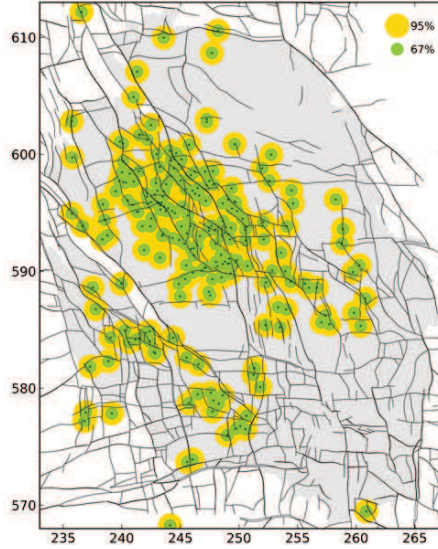


Figure 3: The relationship between observed earthquake epicentres and faults mapped close to the top of the reservoir at the top Rotliegende. Epicentre location errors are denoted by 95% and 67% confidence intervals based on a standard horizontal location error of 500 m.

One possible seismological model developed for the Groningen Field, called the strain partitioning (SP) model, describes the fraction of reservoir strain that is released by earthquakes (Bourne et al., 2014b) leading to a PSHA (Bourne et al., 2014a). This model is based on an empirical stochastic relationship between strain partitioning and reservoir compaction. Kostrov (1974) and McGarr (1976) provide the underlying justification by demonstrating the fundamental connection between the total seismic moment released by a population of earthquakes and the average strain due to those earthquakes. This model is estimated from the reservoir compaction and the seismic moments of earthquakes observed since 1995. Given the importance of the seismological model for assessing seismic hazard and risk, we now seek to develop an alternative model based on an empirical stochastic relationship between the rate of earthquake nucleation and reservoir compaction. Similar approaches have been used to describe injection-induced seismicity (*e.g.* Shapiro et al., 2010, 2013; Mena et al., 2013). This activity rate (AR) model offers a different approach to model parameter estimation and also includes a description of the tendency of events to cluster around previous events as aftershocks.

To begin, we will review the standard formulation of a Poisson point process (Section 2) and then examine a particular instance of this model that

incorporates a linear relationship between reservoir compaction and the nucleation rate of earthquakes (Section 2.2). Deficiencies in this initial simple model motivate a generalisation of the model to incorporate an exponential compaction trend (Section 2.3) to achieve a history match of at least equivalent quality to the SP model. After recognising slight yet significant evidence for event clustering, we will describe an extension of the AR model to include an Epidemic Type Aftershock Sequence (ETAS) model (Section 4). Finally we review the evidence for earthquake nucleation clustering around reservoir compaction and previous earthquakes to determine if there is some residual effects that might be related to earthquakes clustering around pre-existing faults mapped close to the reservoir (Section 5).

2 The Poisson point process model

Following the standard model for point processes (*e.g.* Davison, 2003), suppose we observe events distributed on the time interval $[0, t_0]$ and let $N(w, w+t)$ denote the number of events observed within the sub-interval $(w, w+t)$. If events within disjoint subsets are independent then it follows that the probability of no events within the sub-interval is

$$\Pr\{N(w, w+t) = 0\} = \exp\left(-\int_w^{w+t} \lambda(u)du\right), \quad (3)$$

where $\lambda(u)$ is the intensity function. Since the amount of time, T , from the event at w to the next event exceeds t if and only if $N(w, w+t) = 0$, it follows that the inter-event time, T , is a random variable with a probability density function obtained by differentiating 3 to obtain

$$f_T = -\frac{d\Pr\{N(w, w+t) = 0\}}{dt} = \lambda(w+t) \exp\left(-\int_w^{w+t} \lambda(u)du\right). \quad (4)$$

The joint probability density of n independent events observed at times t_1, \dots, t_n is the product of their respective probability density functions,

$$L = \exp\left(-\int_0^{t_0} \lambda(u)du\right) \prod_{i=1}^n \lambda(t_i). \quad (5)$$

This is also the likelihood expression useful for estimating model parameters from the data. The probability of n events anywhere within the interval $[0, t_0]$ is then the integral of this product with respect to t_1, \dots, t_n and leads to the result

$$\Pr(N(0, t_0) = n) = \frac{\Lambda(t_0)^n}{n!} \exp(-\Lambda(t_0)), \quad (6)$$

where $\Lambda(t_0) = \int_0^{t_0} \lambda(u)du$. The number of events, N , is therefore a Poisson variable with mean $\Lambda(t_0)$.

The conditional probability density, p , that events occur at t_1, \dots, t_n conditional on there being n events within the interval $[0, t_0]$ is (5) divided by (6), *i.e.*

$$p = n! \prod_{i=1}^n \frac{\lambda(t_i)}{\Lambda(t_0)} \quad (7)$$

where $0 < t_1 < \dots < t_n < t_0$. Using Sterling's approximation, $\log(n!) \approx n \log n - n$, this may be computed as

$$\log p = n \log n - n + \sum_{i=1}^n \log \lambda(t_i) - n \log \Lambda(t_0), \quad (8)$$

with negligible error for $n > 100$.

This Poisson process model in one dimension also extends to several dimensions. Consider the case that $\lambda = \lambda(\mathbf{x}, t)$ such that event locations \mathbf{x} are within the bounded region S and occurrence times t are within the interval $[0, t_0]$. The joint probability density of n independent events observed at locations $\mathbf{x}_1, \dots, \mathbf{x}_n$ and times t_1, \dots, t_n follows from (5) as,

$$L = \exp\left(-\int_S \int_0^{t_0} \lambda(\mathbf{x}, t) dS dt\right) \prod_{i=1}^n \lambda(\mathbf{x}_i, t_i). \quad (9)$$

2.1 A homogeneous Poisson point process

In the case of a constant intensity function, $\lambda(\mathbf{x}, t) = \lambda$, the log likelihood for n events follows from (9) as

$$\ell(\lambda) = -At_0\lambda + n \log \lambda, \quad (10)$$

where A is the area of S . Note that in this example the intensity function has units (*e.g.* $\text{km}^{-2} \text{days}^{-1}$), so to ensure the equation is dimensionally correct the log term should be interpreted as $\log(\lambda/\lambda_0)$, where λ_0 is the unit intensity (*e.g.* $1 \text{ km}^{-2} \text{ days}^{-1}$). The maximum likelihood estimate for λ is then found from the derivative of this expression with respect to λ set equal to zero. This yields:

$$\hat{\lambda} = \frac{n}{At_0}. \quad (11)$$

This maximum likelihood estimator is simply the average event rate per unit area. The conditional probability density of observing events at locations $\mathbf{x}_1, \dots, \mathbf{x}_n$ and times t_1, \dots, t_n conditional on there being n events follows from (7) as

$$\frac{n!}{(At_0)^n} \quad (12)$$

2.2 A compaction trend Poisson point process

Let us now consider the case that events preferentially occur in regions of greater absolute reservoir volume change. This suggests an intensity function of the form $\lambda = \alpha \dot{c}$, where \dot{c} is the rate of reservoir compaction with time and α is a constant that describes the number of events per unit reservoir volume change. The likelihood of n events arising at locations $\mathbf{x}_1, \dots, \mathbf{x}_n$ and times t_1, \dots, t_n is

$$L = \exp(-\alpha \Delta V(t_0)) \prod_{i=1}^n \alpha \dot{c}(\mathbf{x}_i, t_i), \quad (13)$$

where $\Delta V(t_0)$ is the absolute reservoir volume change at time t_0 . The log likelihood is

$$\ell = -\alpha \Delta V(t_0) + n \log \alpha + \sum_{i=1}^n \log \dot{c}(\mathbf{x}_i, t_i). \quad (14)$$

This means the maximum likelihood estimate for α is

$$\hat{\alpha} = \frac{n}{\Delta V(t_0)}. \quad (15)$$

From (7), and after generalising this expression from one dimension in time to three dimensions in time and space by including an integral over area, the conditional probability density of observing events at locations $\mathbf{x}_1, \dots, \mathbf{x}_n$ and times t_1, \dots, t_n given there are n events is

$$n! \prod_{i=1}^n \frac{\dot{c}(\mathbf{x}_i, t_i)}{\Delta V(t_0)}. \quad (16)$$

This does not depend on α since it only influences the number of events and not their relative distribution in space and time.

The relative likelihood of the compaction trend model with respect to the homogeneous model is simply the ratio of (16) and (12). The corresponding relative log likelihood is

$$\sum_{i=1}^n \log \dot{c}(\mathbf{x}_i, t_i) - n \log \Delta V(t_0) + n \log At_0. \quad (17)$$

Recognising that $\Delta V(t_0) = \langle \dot{c} \rangle_a At_0$, where $\langle \dot{c} \rangle_a$ is the arithmetic average rate of reservoir thickness change over the spatial interval S and the time interval $[0, t_0]$, this expression simplifies to

$$\sum_{i=1}^n \log \dot{c}(\mathbf{x}_i, t_i) - n \log \langle \dot{c} \rangle_a, \quad (18)$$

The relative likelihood is therefore:

$$\left(\frac{\langle \dot{c} \rangle_g}{\langle \dot{c} \rangle_a} \right)^n, \quad (19)$$

where $\langle \dot{c} \rangle_g$ is the geometric average rate of reservoir compaction at the time and location of each event. This means the relative likelihood simply depends on the ratio of the geometric mean compaction rate for the events and the arithmetic mean compaction rate for the reservoir.

Based on the observed distribution of $M \geq 1.5$ earthquake epicentres and reservoir compaction between 1995 and 2013 in the Groningen Field (Figure 1), application of (19) yields a relative likelihood of 7×10^{14} . This suggests epicentres are significantly more likely to be located in regions of greater compaction than could be expected simply due to chance that would distribute events with equal likelihood anywhere within the reservoir. Figure 4 shows the cumulative number of events, n as a function of reservoir volume decrease, ΔV . According to (15), the data should plot with a constant slope equal to $\hat{\alpha}$, however the slope clearly increases with ΔV . Based on the Kolmogorov-Smirnov test statistic the compaction-trend Poisson Point Process model may be rejected within greater than 99% confidence. Figure 5 shows the map distribution of local estimates for the number of events per unit volume change. These were obtained as the ratio of the event density map (Figure 1b) to the reservoir compaction map (Figure 1a). This again indicates the larger intensities cluster around the larger values of reservoir compaction.

Furthermore, estimates for $\hat{\alpha}$ within disjoint intervals of reservoir compaction (Figure 6) show an approximate exponential increase in $\hat{\alpha}$ with respect to compaction. This suggests an alternative Poisson Point Process model based on an exponential compaction trend. Given the limited range in observed compaction values, alternative parametrizations, such as an inverse power-law, are also similarly consistent with the data. As the current data do not allow us to distinguish between these alternatives, we choose for now to proceed with the exponential trend parametrization.

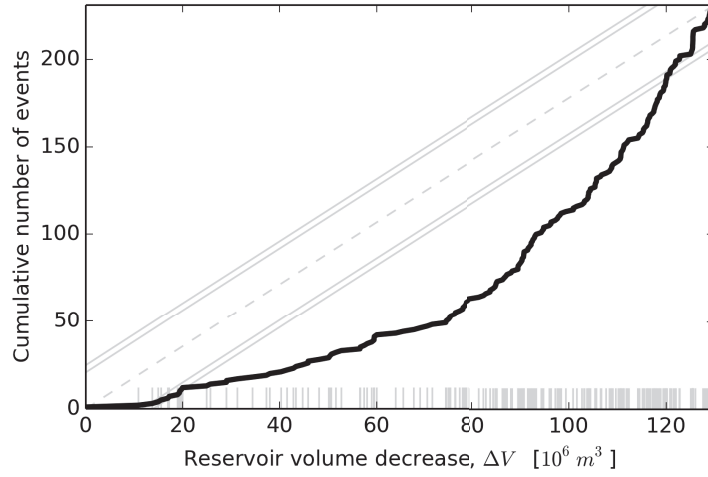


Figure 4: The observed cumulative distribution of events with reservoir volume decrease relative to a homogeneous Poisson process. The model bounds denote the 0.95 and 0.99 quantiles of the Kolmogorov-Smirnov test statistic. Tick marks denote each individual event.

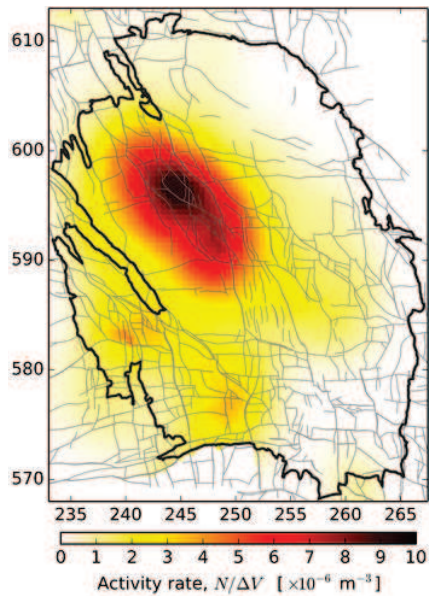


Figure 5: The map distribution of maximum likelihood estimates for the activity rate, $\hat{\alpha}$, suggests a trend with reservoir compaction.

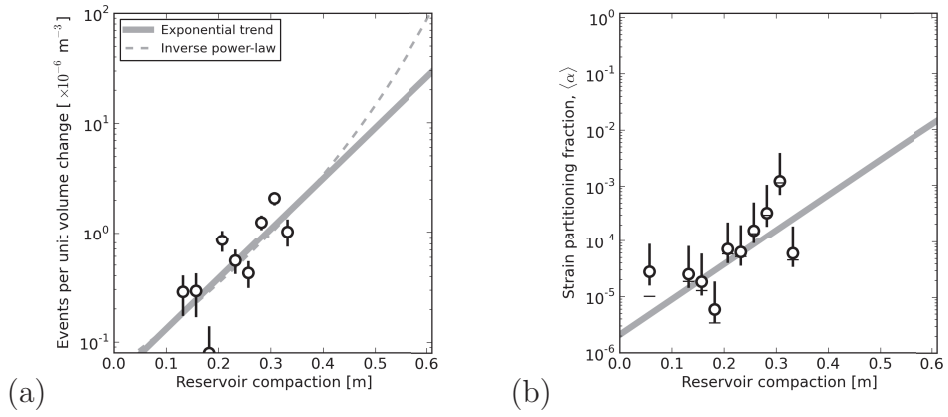


Figure 6: (a) The number of $M \geq 1.5$ events per unit reservoir volume decrease increases with an approximate exponential trend relative to reservoir compaction. (b) The exponential-like trend of strain partitioning with compaction is subject to considerably more variability.

2.3 An exponential compaction trend Poisson process

Motivated by the observed trend in Figure 6, let us now consider an exponential trend Poisson point process model as a function of reservoir compaction, $c(t)$, of the form:

$$\frac{\Lambda(S, t)}{\Delta V(S, t)} = \beta_0 e^{\beta_1 \bar{c}}, \quad (20)$$

where $\Lambda(S, t)$ is the expected number of events within the region S and the time period $(0, t)$, $\Delta V(S, t)$ is the bulk reservoir volume decrease within the region S at time t , and

$$\bar{c} = \frac{1}{A} \int_S c dS, \quad (21)$$

where A is the area of region S . This is a two-parameter model, where β_0 describes the background activity rate and β_1 describes the exponential increase in activity rate with compaction. Recognising that $\Delta V = Ac$, where A is the surface area of the reservoir subject to compaction, c , leads to

$$\Lambda = Ac\beta_0 e^{\beta_1 c}. \quad (22)$$

Now, we seek a Poisson intensity function of the form, $\lambda = \lambda(\mathbf{x}, t)$, such that, $\Lambda(t_0) = \int_S \int_0^{t_0} \lambda(\mathbf{x}, t) dS dt$ and also for subsets of S selected to contain approximately constant compaction then the expected number of events, Λ , follows equation 22. This implies

$$\lambda(\mathbf{x}, t) = \beta_0 \dot{c} (1 + \beta_1 c) e^{\beta_1 c}, \quad (23)$$

where $c = c(\mathbf{x}, t)$, $c(\mathbf{x}, 0) = 0$, $\dot{c} = dc/dt$, and so it follows that

$$\Lambda(t_0) = \int_S \beta_0 c(\mathbf{x}, t_0) e^{\beta_1 c(\mathbf{x}, t_0)} dS. \quad (24)$$

Consider for a moment, the special case of a small subset of the reservoir where c is approximately constant. From (7) it follows that the probability density function for a single event within the time interval $(0, t_0)$ is

$$\frac{\lambda(t)}{\Lambda(t_0)} = \frac{\dot{c}(1 + \beta_1 c)}{Ac_0} e^{\beta_1(c-c_0)}. \quad (25)$$

This indicates an exponential skew in the distribution of event origin times towards the end of the time interval within this part of the reservoir. Consequently events are more likely to occur towards the end of the time interval. A similar exponentially skewed distribution exists for the general case of $c = c(\mathbf{x}, t)$.

The log-likelihood of n independent events observed at locations $\mathbf{x}_1, \dots, \mathbf{x}_n$ and occurrence times t_1, \dots, t_n within the region S and the time period $(0, t_0)$ follows from (9) as,

$$\ell = -\Lambda(t_0) + \sum_{i=1}^n \log \lambda(\mathbf{x}_i, t_i). \quad (26)$$

Combining (26), (23) and (24) leads to

$$\begin{aligned} \ell = & - \int_S \beta_0 c(\mathbf{x}, t_0) e^{\beta_1 c(\mathbf{x}, t_0)} dS + n \log \beta_0 \\ & + \sum_{i=1}^n \log(1 + \beta_1 c(\mathbf{x}_i, t_i)) + \beta_1 \sum_{i=1}^n c(\mathbf{x}_i, t_i) + \sum_{i=1}^n \log \dot{c}(\mathbf{x}_i, t_i) \end{aligned} \quad (27)$$

If earthquake observations only started at time t_s after some initial period of reservoir compaction $(0, t_s)$ then the log-likelihood of n independent events observed at locations $\mathbf{x}_1, \dots, \mathbf{x}_n$ and occurrence times t_1, \dots, t_n within the region S and the time period (t_s, t_0) is

$$\begin{aligned} \ell = & - \int_S \beta_0 (c(\mathbf{x}, t_0) e^{\beta_1 c(\mathbf{x}, t_0)} - c(\mathbf{x}, t_s) e^{\beta_1 c(\mathbf{x}, t_s)}) dS \\ & + n \log \beta_0 + \sum_{i=1}^n \log(1 + \beta_1 c(\mathbf{x}_i, t_i)) + \beta_1 \sum_{i=1}^n c(\mathbf{x}_i, t_i) + \sum_{i=1}^n \log \dot{c}(\mathbf{x}_i, t_i) \end{aligned} \quad (28)$$

In either case, maximum likelihood estimates for the model parameters (β_0, β_1) may be obtained by maximising (27) with respect to β_0 and β_1 . In the general case of $c = c(\mathbf{x}, t)$, this requires numerical integration and optimisation methods. Notice, however, that these maximum likelihood estimates do not depend on the rate of compaction, \dot{c} , as the last term in (27) is a constant.

To evaluate the log-likelihood function, numerical integration of the compaction model is required at two moments in time, at the start of the earthquake observation (t_s) , and at the end of the observation period (t_0) . In addition, the value of compaction at the location and occurrence time of each event must be obtained. Typically the reservoir compaction model is evaluated on a discrete grid in space and time. This means that estimates for compaction at times $t_s, t_1, \dots, t_n, t_0$ must be obtained by interpolation from the times available within the model, t_k . For now, we choose to proceed using simple piece-wise linear interpolation in time.

2.3.1 Maximum likelihood parameter estimates

Maximum likelihood estimates for β_0, β_1 were obtained numerically using the Nelder and Mead (1965) simplex algorithm to minimise the negative

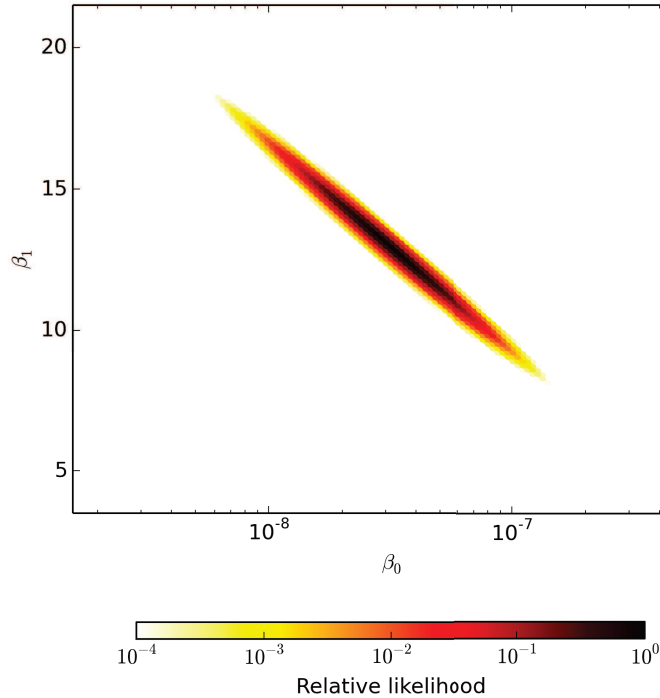


Figure 7: Relative likelihood of the exponential compaction trend Poisson Point Process model explaining the observed $M \geq 1.5$ earthquake distribution in relation to the reservoir compaction model from April 1995 to September 2014. The maximum likelihood solution is $\hat{\beta}_0 = 3.09 \times 10^{-8}$ and $\hat{\beta}_1 = 13.03$. Variation in relative likelihood around this solution provides an estimate of the confidence interval.

log-likelihood expression given by (28). Using the catalogue of $M \geq 1.5$ earthquakes observed between April 1995 and August 2014 and the Time-decay reservoir compaction model yields a maximum likelihood estimate of $\hat{\beta}_0 = 3.09 \times 10^{-8}$ and $\hat{\beta}_1 = 13.03$. Values of relative likelihood evaluated within the vicinity of this solution indicate uncertainty in this estimate. As expected, due to the limited number of earthquakes and limited range of reservoir compaction, there is a clear trade-off between $\hat{\beta}_0$ and $\hat{\beta}_1$. Nonetheless, the possibility of no covariance between seismicity and compaction may be confidently rejected given $\hat{\beta}_0 > 0$. Consistent with the previous analysis, a simple linear relationship between seismicity and compaction also may be confidently rejected given $\hat{\beta}_1 > 0$.

2.3.2 Extension to a Marked Poisson Point Process

The number of observed earthquakes, N , of at least magnitude, M , within a given region and period of time follow the log-linear frequency-magnitude relationship known as the Gutenberg-Richter law (Gutenberg and Richter, 1954):

$$\log_{10} N(M) = a - bM. \quad (29)$$

The b parameter, known as the b -value, describes the relative decline in abundance of larger earthquakes relative to smaller ones and is therefore central to estimating the probability of larger earthquakes from an observed population of earthquakes. For a monitoring system with a magnitude threshold for detection and location of M_{min} (magnitude of completeness) the corresponding probability density is

$$f(M|M \geq M_{min}) = b'e^{-b'(M-M_{min})} \quad (30)$$

where $b' = b \log 10$. This distribution is however not physical as there is no finite upper bound to the distribution. Instead, a truncated distribution is preferred such as proposed by Cornell and Vanmarcke,

$$f(M|M \geq M_{min}) = \beta \frac{e^{-\beta(M-M_{min})} - e^{-\beta(M_{max}-M_{min})}}{1 - e^{-\beta(M_{max}-M_{min})}}, \quad (31)$$

where $\beta = b'/d$, $d = 1.5$, and M_{max} is the maximum possible magnitude.

Groningen seismicity provides no empirical evidence for a maximum magnitude that truncates the frequency-magnitude distribution (Figure 8). However one must exist to represent the upper bound on the total amount of strain energy available. Instead M_{max} may be estimated using geomechanical principles under the assumption that the induced seismicity only accommodates induced strain due to reservoir compaction (see Bourne et al., 2014b). In this way, the total induced strain available at the end of gas production provides a clear physical upper bound to the maximum magnitude. Starting with the fundamental relationship between the average strain due to a population of earthquakes and their total seismic moment (Kostrov, 1974), this leads to an upper bound on total seismic moment according to the absolute value of the ultimate bulk reservoir volume change, $|\Delta V|$, such that

$$M_o = 2\mu|\Delta V|, \quad (32)$$

This expression is comparable to that obtained by McGarr (1976) for a range of specific particular deformation geometries associated with subsurface volume changes. The maximum total seismic moment computed for the Groningen Field is 7×10^{18} Nm. The relationship between the magnitude, M , and the seismic moment, M_o , takes the form (Hanks and Kanamori, 1979).

$$\log_{10} M_o = c + dM, \quad (33)$$

where typically $c = 9.1$ and $d = 1.5$. Hence the maximum total seismic moment corresponds to $M_{max} = 6.5$ (Bourne et al., 2014b).

An analytic expression for the maximum likelihood estimate of the b -value given a catalogue of event magnitudes was derived by Aki (1965) and Utsu (1966). This follows from the log-likelihood as a function of the b -value given the observed magnitudes M_1, \dots, M_n , as

$$\ell = n \log b' - b' \sum_{i=1}^n (M_i - M_{min}). \quad (34)$$

Note that this excludes any contribution from M_{max} which cannot be reliably estimated from the historic seismicity Bourne and Oates (2012) due to the limited number of larger magnitude events.

The maximum likelihood b -value estimate is therefore

$$b = \frac{1}{\ln 10 (\langle M \rangle - M_{min})} \quad (35)$$

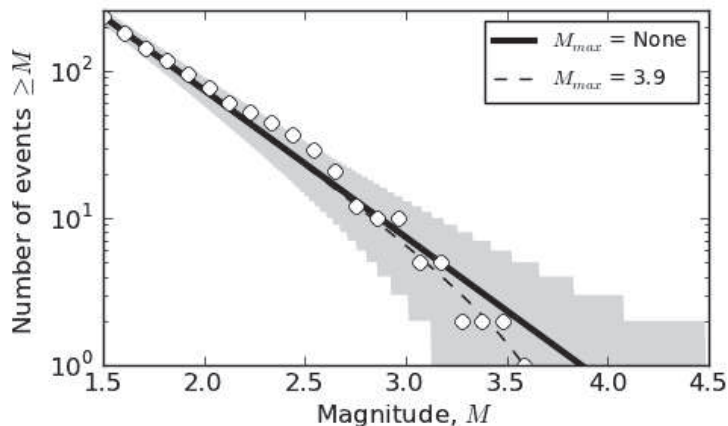


Figure 8: The frequency-magnitude distribution of $M \geq 1.5$ events observed within the Groningen Field between April 1995 and September 2014 are consistent with a power-law distribution that is typically observed for most forms of natural and induced seismicity. The slope of this distribution, the b -value, is consistent with the typical value of $b = 1$. Grey shading denotes the 95% confidence interval around this model. The dashed line shows a truncated frequency-magnitude distribution (see equation 31) with $M_{max} = 3.9$. Given the confidence interval this improved fit is not statistically significant.

where $\langle M \rangle$ is the mean magnitude. If this Aki-Utsu equation is used in its original form the b -values obtained give a noticeably different fit to the frequency-magnitude data than regression methods. This discrepancy is due to the finite width of the magnitude bins used, as pointed out by Marzocchi and Sandri (2003), among others, and may be corrected by replacing M_{min} by $M_{min} - \Delta M/2$. If bins of width ΔM are used, the first magnitude bin contains events with magnitudes $M_{min} - \Delta M/2 < M \leq M_{min} + \Delta M/2$ Marzocchi and Sandri (2003).

2.3.3 A stochastic simulation procedure

A simulation procedure is required to compute the number of events, and the location, origin time and magnitude for each individual event for each stochastic realisation of the earthquake catalogue within the period (t_s, t_0) .

The number of events is computed as a single sample from the Poisson distribution with a mean value equal to

$$\Lambda(t_0) - \Lambda(t_s) = \beta_0 \int_S c(\mathbf{x}, t_0) e^{\beta_1 c(\mathbf{x}, t_0)} - c(\mathbf{x}, t_s) e^{\beta_1 c(\mathbf{x}, t_s)} dS \quad (36)$$

The event locations are computed by sampling the expected event density function, $N(\mathbf{x})$, defined as the expected number of events per unit area, *i.e.*

$$N(\mathbf{x}) = \beta_0 (c_0 e^{\beta_1 c_0} - c_s e^{\beta_1 c_s}) \quad (37)$$

where c_s, c_0 denote the compaction at location \mathbf{x} at times t_s and t_0 respectively.

The origin time of an event at a given location may be obtained by sampling the cumulative probability distribution, $F(t)$, such that

$$F(t) = \frac{c_t e^{\beta_1 c_t} - c_s e^{\beta_1 c_s}}{c_0 e^{\beta_1 c_0} - c_s e^{\beta_1 c_s}} \quad (38)$$

where c_t, c_s, c_0 denote the compaction at location \mathbf{x} at times t, t_s and t_0 respectively.

Earthquake magnitudes are simulated as independent samples from a truncated Pareto frequency-magnitude distribution

$$F(M|M \geq M_{min}) = \frac{e^{-\beta(M-M_{min})} - e^{-\beta(M_{max}-M_{min})}}{1 - e^{-\beta(M_{max}-M_{min})}} \quad (39)$$

where $\beta = b'/d$ with $b = 1$, $M_{min} = 1.5$, and $M_{max} = 6.5$. This maximum magnitude is then adjusted after every simulated earthquake to ensure the total seismogenic strain cannot exceed the total reservoir strain, *i.e.*

$$M_{max} = d \log_{10}(M_{o,max} - M_{o,sim}) - c \quad (40)$$

where $M_{o,max} = 7 \times 10^{18}$ Nm and $M_{o,sim}$ is the total seismic moment of all the previous earthquakes within the simulated earthquake catalogue.

2.3.4 Stochastic simulation of historic seismicity

Comparing the results of stochastic simulations with observed seismicity is essential to assess their validity and to identify any opportunities for further improvement.

Figure 9(a-d) shows such a comparison for the temporal and spatial distribution of event numbers and total seismic moments obtained after some 10,000 earthquake catalogues were simulated for the period April 1995 to August 2014. The temporal distribution of seismicity is measured by the total number and total seismic moment occurring anywhere within the field as it increases with time since the start of the period in April 1995. Likewise the spatial distribution is indicated by the total number and total seismic moment occurring at any time within the period as it increases with distance from the centroid of the observed epicentres. In all cases the spread of simulation results are represented by the median value and the 95% confidence interval around this median value. As expected, cumulative event numbers show a symmetric Poisson distribution about the median and total seismic moments show an asymmetric Pareto sum distribution with the upper confidence bound substantially further from the median than the lower confidence bound.

There is good agreement between the observed and simulated temporal distribution of event numbers (Figure 9a), and similarly so for the temporal and spatial distributions of total seismic moment. However we do note that the median total seismic consistently exceeds the observed values through time, and there is also a transient exceedance below the 95% confidence bound in 2003. This suggests the possibility of a slight upward bias in the model meaning it systematically over-predicts the total seismic moment. One way to reduce this bias would be to increase the b -value as this would lower the median total seismic moment without changing the median total event numbers. This is worthy of further investigation as it may be possible to achieve this improvement whilst maintaining the simulated b -value within the margin of uncertainty around the b -value estimated from the observed earthquakes, $b = 1 \pm 0.2$ (Bourne and Oates, 2012).

The most significant difference between the observed and simulated earthquakes is the spatial spread of event numbers (Figure 9b). The observed events are more localised around the centroid of seismicity than the simulated events by 3 ± 1 km. This discrepancy is small compared to the 40 km length of the field. This indicates that out of the potential spatial variabil-

ity of epicentres within the field (*i.e.* ± 20 km) most is explained by the activity rate model based on compaction (85%). This does however leave some residual variability (15%) still to be modelled, perhaps by improving the compaction model through better quantification of uncertainty in the model after fitting the geodetic subsidence data, or through understanding the extent to which earthquakes are localised on mapped faults.

Finally, we note that the distribution of times and distances between consecutive events (Figure 9e,f) reveal a consistent and statistically significant model discrepancy of over-dispersion. In particular, the observed earthquakes show a greater abundance of events within 3-10 days and 1-10 km of each other than the model. This suggests that some of the earthquakes may be aftershocks triggered by previous earthquakes.

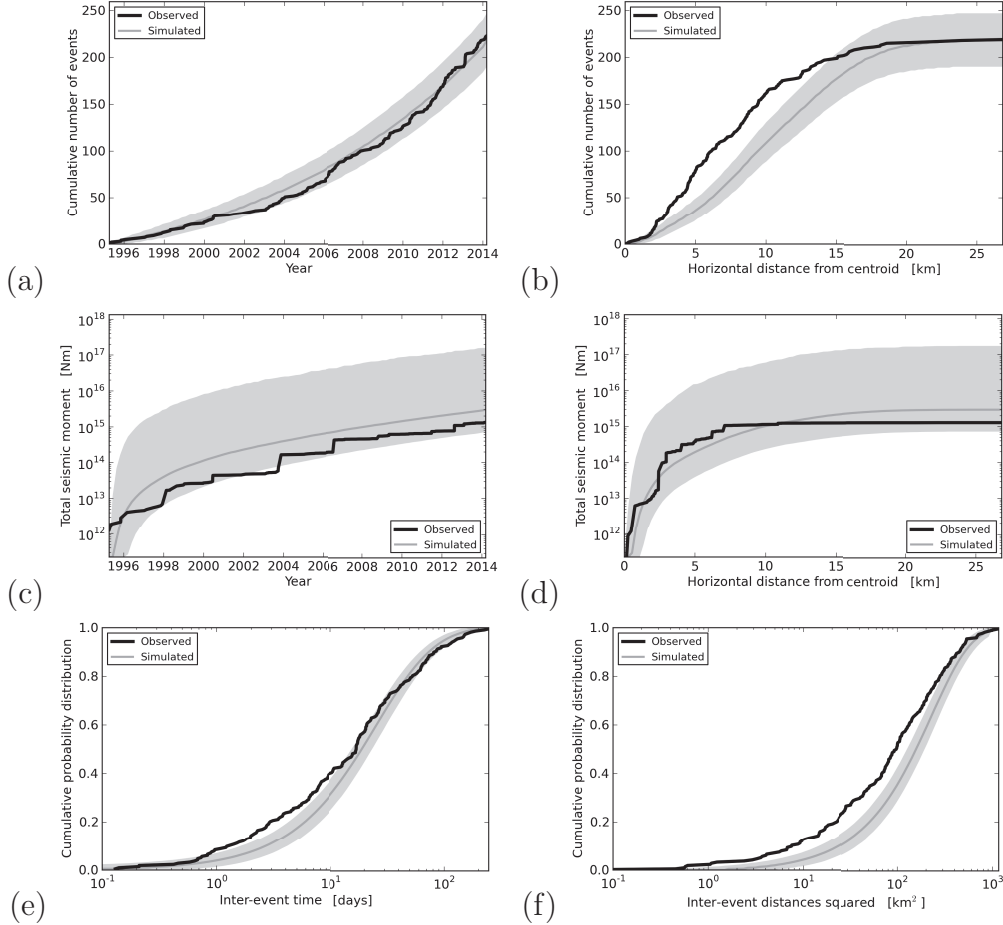


Figure 9: Simulation results from the exponential compaction trend Poisson process model. (a) The cumulative number of $M \geq 1.5$ events observed through time between April 1995 and August 2014 as a function of time. (b) As (a) except for the horizontal distance from the centroid of the observed locations. (c, d) As (a, b) except for total seismic moment. (e, f) The inter-event times and distances-squared provide a measure of temporal and spatial clustering respectively. The simulated results are shown as the median and the 95% confidence interval. These results were obtained from 10,000 catalogues simulated according to the exponential compaction trend Poisson model and a standard random location error of 500 m. Model parameter estimates were sampled from the relative likelihood distribution shown in Figure 7. In this case the simulations are based on independent samples from a frequency-magnitude distribution with $b = 1$, $M_{min} = 1.5$, $M_{max} = 6.5$ initially, and a standard magnitude error of 0.2.

3 Earthquake clustering

3.1 Aftershocks and temporal clustering

Figure 9e indicates the observed earthquakes are significantly more clustered in time than the maximum likelihood Poisson point process model. This is noticeable by the over abundance of events with inter-event times of less than 20 days. Differencing the Poisson model from the observed probability density distribution, *i.e.* differentiate the black and grey curves shown in Figure 9e and differencing them, provides a measure of the inter-event temporal trigger function (Figure 10) which provides a reasonable fit with Omori's Law (inverse power-law) for a power-law exponent of 1.45 and a characteristic time of 3 days.

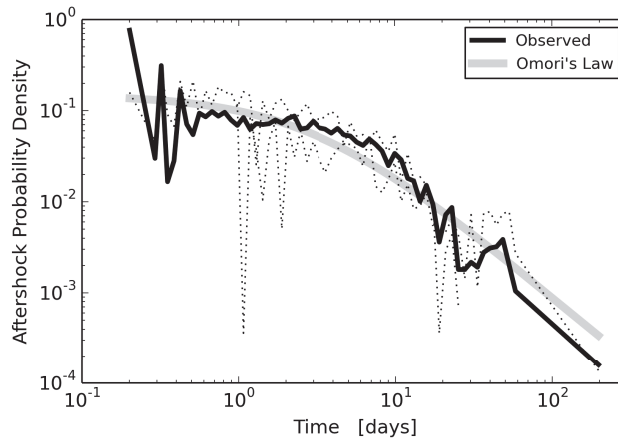


Figure 10: Aftershock probability density as a function of time after the main event. This was estimated as the difference between the observed probability density and estimates of the probability density for independent events. The latter was based on the maximum likelihood estimate for the exponential compaction trend Poisson point process. Dashed lines denote the 95% confidence interval in the observed distribution. For comparison, Omori's Law for aftershocks is shown for $p = 1.45$ and $c = 3$ days.

3.2 Aftershocks and spatial clustering

The frequency distribution of inter-event distances (Figures 9f) indicates the observed earthquakes exhibit a small yet significant under-dispersion compared to the Poisson point model of independent event locations. Figure 11 shows further information about the nature of spatial clustering of aftershock epicentres. Events that occur within 3 days of each other are more likely than not to be located with 10 km of each other (Figure 11c). Although, there is no clear evidence at present for any significant anisotropy in the distribution of spatial clustering (Figure 11b).

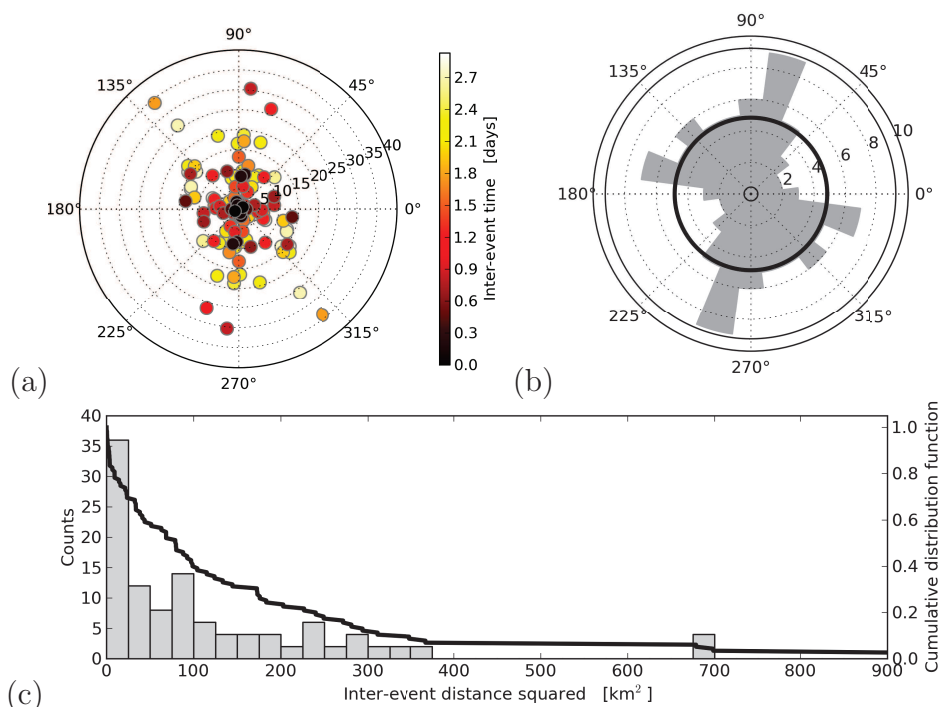


Figure 11: Evidence for spatial clustering of aftershocks. (a) The horizontal offset vectors between all event pairs within 3 days of each other expressed as polar angles in degrees and distance in kilometres. (b) The frequency distribution of these offset azimuths. Black solid lines denote the expected value and the 95% confidence interval for an isotropic distribution. (c) The frequency distribution of these offset distances.

3.3 Aftershock productivity

If we identify potential aftershocks as those events occurring within 3 days of a previous event, then there is some evidence that aftershock productivity (average number of aftershocks per main event) increases with the magnitude of the main event (Figure 12a). Although, given the small number of observed aftershocks this apparent trend remains somewhat uncertain and may change as more data are acquired. This trend is consistent with a power-law although due to the observed scatter about this trend there is some significant uncertainty about the value of the power-law exponent. The frequency-magnitude distribution of these aftershocks (Figure 12b) has a b -value that is indistinguishable from the b -value for the entire earthquake population, where $b = 1$ (*e.g.* Bourne and Oates, 2012). Furthermore, the frequency distribution of magnitude differences between the main shock and its aftershocks shows most but not all aftershocks are smaller than the magnitude of the main shock. Both of these results are consistent with event magnitudes occurring independently of previous event magnitudes – that is there is no evidence of aftershock magnitudes depending on the magnitude of the main event.

These observations of significant spatial and temporal correlations between events but no correlation between event magnitudes are also typical of naturally occurring seismicity. Motivated by this similarity, we will now consider a general model for such inter-event correlations in natural earthquakes known as the Epidemic Type Aftershock Sequence model.

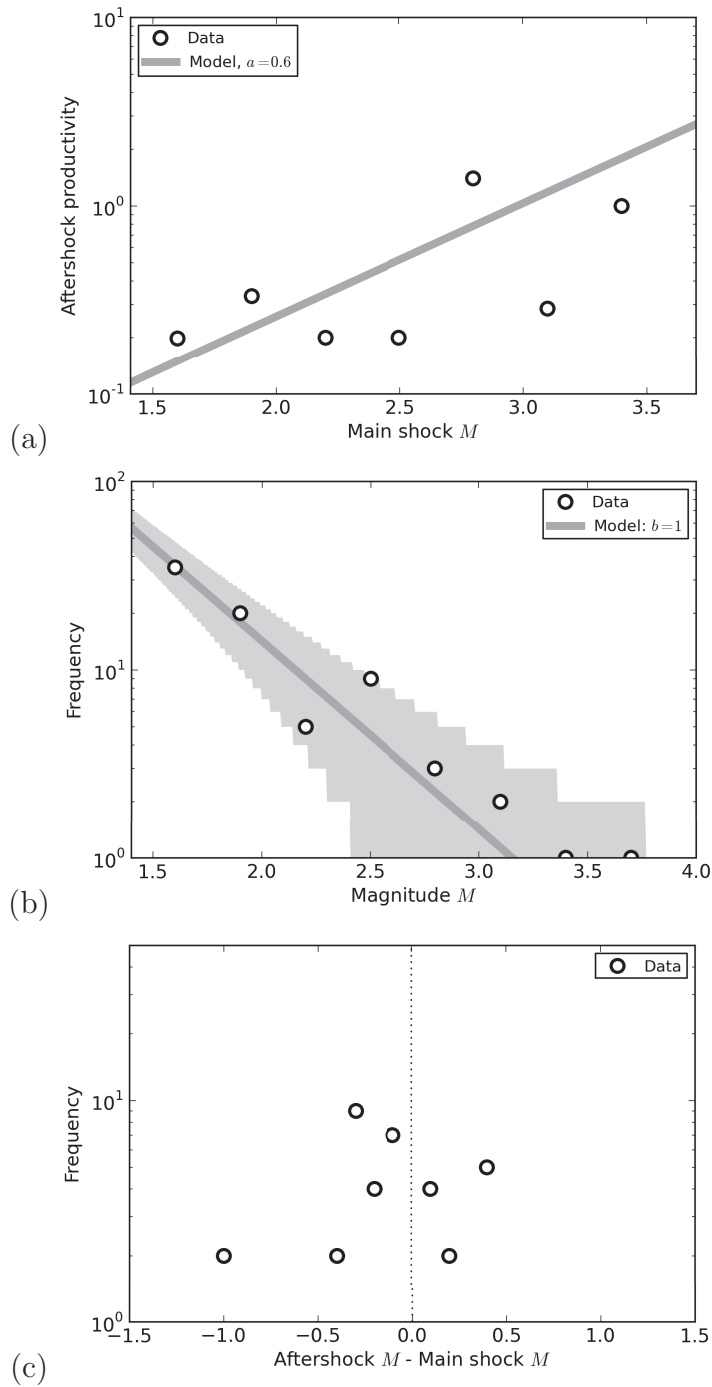


Figure 12: (a) The average number of $M \geq 1.5$ aftershocks per main shock. (b) The frequency-magnitude distribution of aftershocks. (c) The frequency distribution of magnitude differences between the main shock and an aftershock. Aftershocks were identified as events within 3 days of a previous event.

4 The Epidemic Type Aftershock Sequence Model

Treating the seismological model as a point process with conditional intensity λ , the log-likelihood given the time-ordered sequence of observed events (t_i, \mathbf{x}_i) follows from (9) as

$$\ell = - \int_S \int \lambda(t, \mathbf{x}) dS dt + \sum_{i=1}^n \log \lambda(t_i, \mathbf{x}_i) \quad (41)$$

According to the Epidemic Type Aftershock Models Ogata (1998, 2011), the conditional intensity λ is expressed as

$$\lambda(\mathbf{x}, t) = \lambda_p + \sum_{j=1}^{i-1} f(t_i - t_j, \mathbf{x}_i - \mathbf{x}_j | M_j) \quad (42)$$

where λ_p is the intensity function for independent events, M_j is the magnitude of the j^{th} event, and $t_i, t_j, \mathbf{x}_i, \mathbf{x}_j$ are the origin times and locations of the i^{th} and j^{th} events respectively. Function f is the aftershock triggering function defined as

$$f = K g(t) h(r) e^{a(M-M_0)} \quad (43)$$

where t is the inter-event time, r is the inter-event distance, M is the event magnitude, M_0 is the minimum magnitude, and K, a are parameters of the ETAS model. The functions $g(t)$ and $h(r)$ are the probability density functions for temporal and spatial triggering defined as:

$$g(t) = \frac{(p-1)}{c} \left(\frac{t}{c} + 1 \right)^{-p} \quad (44)$$

$$h(r) = \frac{(q-1)}{\pi d} \left(\frac{r^2}{d} + 1 \right)^{-q} \quad (45)$$

and $r^2 = x^2 + y^2$, $\mathbf{x} = (x, y)$, c, p are the characteristic time and temporal power-law exponent parameters, and d, q are the characteristic area and spatial power-law exponent parameters of the ETAS model. The corresponding cumulative probability density functions for temporal and spatial triggering follow by integration as

$$G(t) = 1 - \left(\frac{t}{c} + 1 \right)^{1-p} \quad (46)$$

$$H(r) = 1 - \left(\frac{r^2}{d} + 1 \right)^{1-q} \quad (47)$$

Similarly, the expected number of aftershocks directly triggered by a single event of magnitude M is

$$K e^{a(M-M_0)}. \quad (48)$$

Given the physical requirement for the total number of events in any aftershock sequence to be positive definite and finite

$$0 \leq K e^{a(M-M_0)} < 1. \quad (49)$$

Next, let us consider maximum likelihood estimation of the model parameters. Starting with the simple illustrative example of a homogeneous Poisson point process, *i.e.* constant intensity $\lambda_p = \mu$, and a magnitude-independent ETAS process, *i.e.* $a = 0$. The log-likelihood function may be expressed as

$$\ell = -\mu AT(1 + K) + \sum_{i=1}^n \log(\mu + K g_i h_i). \quad (50)$$

where A and T are the area and time period of observation and $g_i = g(t_i)$, $h_i = h(r_i)$. The first term on the right hand side makes use of Schoenberg's approximation for the integral contribution from the ETAS model that assumes the trigger function is negligible outside the area and time period of observation Schoenberg (2013).

After differentiation and rearrangement, the following expressions for maximum likelihood estimates of μ and K may be obtained

$$AT(1 + \hat{K}) = \sum_{i=1}^n \frac{1}{\hat{\mu} + \hat{K} g_i h_i} \quad (51)$$

$$\hat{\mu} AT = \sum_{i=1}^n \frac{g_i h_i}{\hat{\mu} + \hat{K} g_i h_i}. \quad (52)$$

In the limit of weak event triggering, such that $K g_i h_i \ll \mu$ for all i , these expressions may be simplified to yield

$$\hat{\mu} = \sqrt{\hat{\mu}_0 \langle gh \rangle} \quad (53)$$

$$1 + \hat{K} = \sqrt{\frac{\hat{\mu}_0}{\langle gh \rangle}} \quad (54)$$

$$\hat{\mu}_0 = \frac{n}{AT}, \quad (55)$$

where $\langle gh \rangle$ is the average value of the triggering function for all observed events. Here, μ_0 is recognisable as the maximum likelihood estimate for the rate of independent events in the limit of no aftershocks. Also notice that there is a trade-off between the estimates for μ and K ; this is clearly seen by eliminating $\langle gh \rangle$ from the previous expressions to obtain $\hat{\mu}(1 + \hat{K}) = \hat{\mu}_0$, where $\hat{\mu}_0$ is a constant.

4.1 Joint parameter estimation

Joint maximum likelihood estimates for the exponential compaction trend Poisson process model (β_0, β_1) and the ETAS model (K, p, c, q, d, a) were obtained numerically using the Nelder and Mead (1965) simplex algorithm to minimise the negative log-likelihood expression for the historic seismicity and reservoir compaction data. The resulting parameters estimates are $\{\beta_0, \beta_1, K, a, p, c, q, d, a\} = \{2.3 \times 10^{-8}, 12.8, 0.31, 1.45, 3.0, 1.9, 5 \times 10^6, 0.6\}$. These were obtained subject to the constraint that $c = 3$ days since this parameter is only weakly constrained by the small number of historic events.

Figure 13 indicates the solution space according to the relative likelihood of the historic data arising from the model. This provides an impression of the confidence intervals for each parameter and the null-space due to trade-off between some parameters leaving the fit of the model to the data essentially unaffected. As expected from the previous discussion, there is a negative covariance between $\{K, \beta_0\}$ and $\{K, \beta_1\}$. The parameters $\{K, a\}$ also exhibit a pronounced negative covariance; these are expected to be coupled since the expected number of aftershocks is $Ke^{a(M-M_0)}$.

The lower right two plots in Figure 13 reveal unbounded null spaces for $\{p, c\}$ and $\{q, d\}$. This occurs because although the observed aftershocks exhibit significant temporal and spatial clustering there are too few of them to uniquely constrain the spatial and temporal triggering functions since most aftershocks are observed within just 3 days and 10 km of the main event. With continued monitoring it is likely that the future earthquake catalogues will contain more aftershocks at greater times and distances from the main events to allow more precise estimates of p, c, q, d .

For now we choose to obtain the maximum likelihood parameter estimates subject to the constraint $c = 3$ days which is consistent with the earlier graphical analysis. Uncertainty in these maximum likelihood values is then represented by a list of acceptable parameter combinations computed using Monte Carlo sampling of the relative likelihood function. This set of parameter combinations is then available to be re-sampled during stochastic simulations of earthquake catalogues.

Finally we note that any attempt to de-cluster the earthquake catalogue in

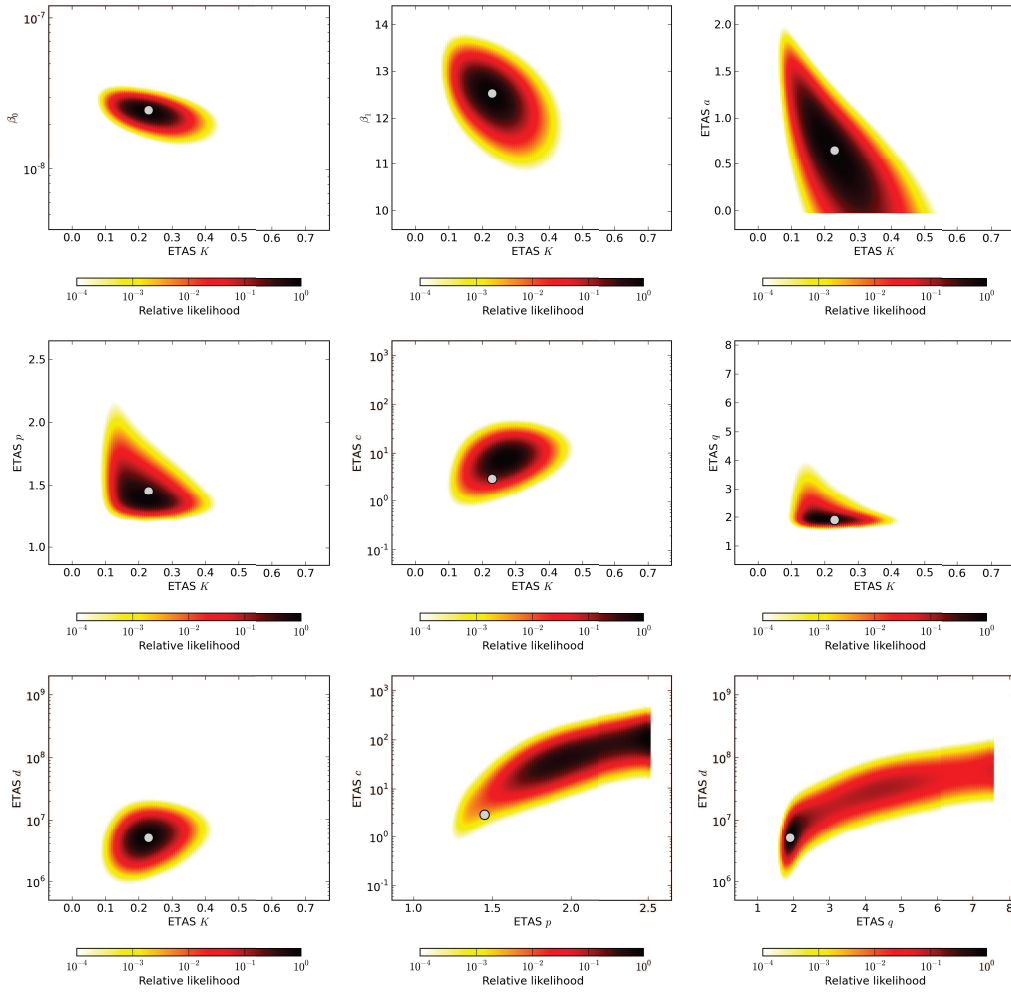


Figure 13: A selection of slices through the relative likelihood distribution around the maximum likelihood parameter estimates. White dots denote the maximum likelihood parameter estimates for $\beta_0, \beta_1, K, p, q, d$ subject to the constraint $c = 3$ days.

order to obtain unbiased estimates of Poisson model parameters is fraught with ambiguity. The intensity distributions of independent events and aftershocks are frequently too similar to allow any single event to be confidently labelled as an independent event or a triggered event (Figure 14). This difficulty is avoided by joint estimation of the independent and triggered event process parameters as previously described, and then joint simulation of main shocks and aftershocks.

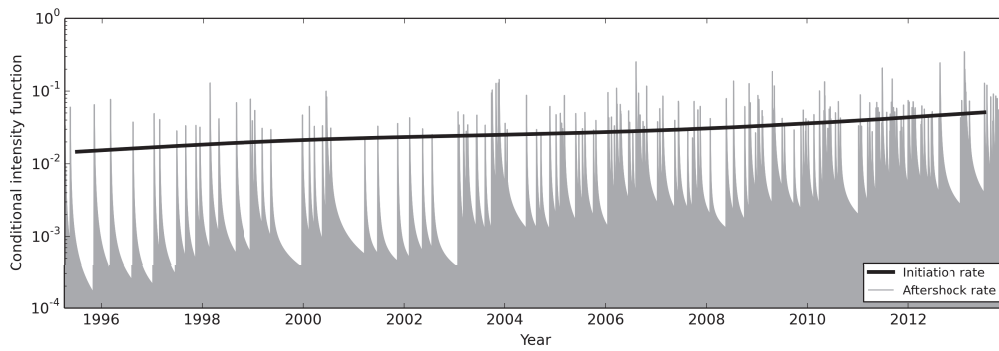


Figure 14: Intensity functions for the background initiation and aftershock triggering rates for the observed events. These functions are based on the joint maximum likelihood estimates obtained for the exponential compaction trend model with ETAS.

4.2 Simulation of historic events

As before, we now seek to assess how the inclusion of an epidemic type aftershock sequence model improves the performance relative to the observed seismicity (Figure 15). Notably the observed temporal and spatial cluster of consecutive events is now well-explained by the model within tight confidence bounds (Figure 15e,f). Relative to the previous activity rate model without aftershocks, the confidence bound on event numbers has also widened, primarily due to the upper bound increasing (Figure 15a,b). This departure

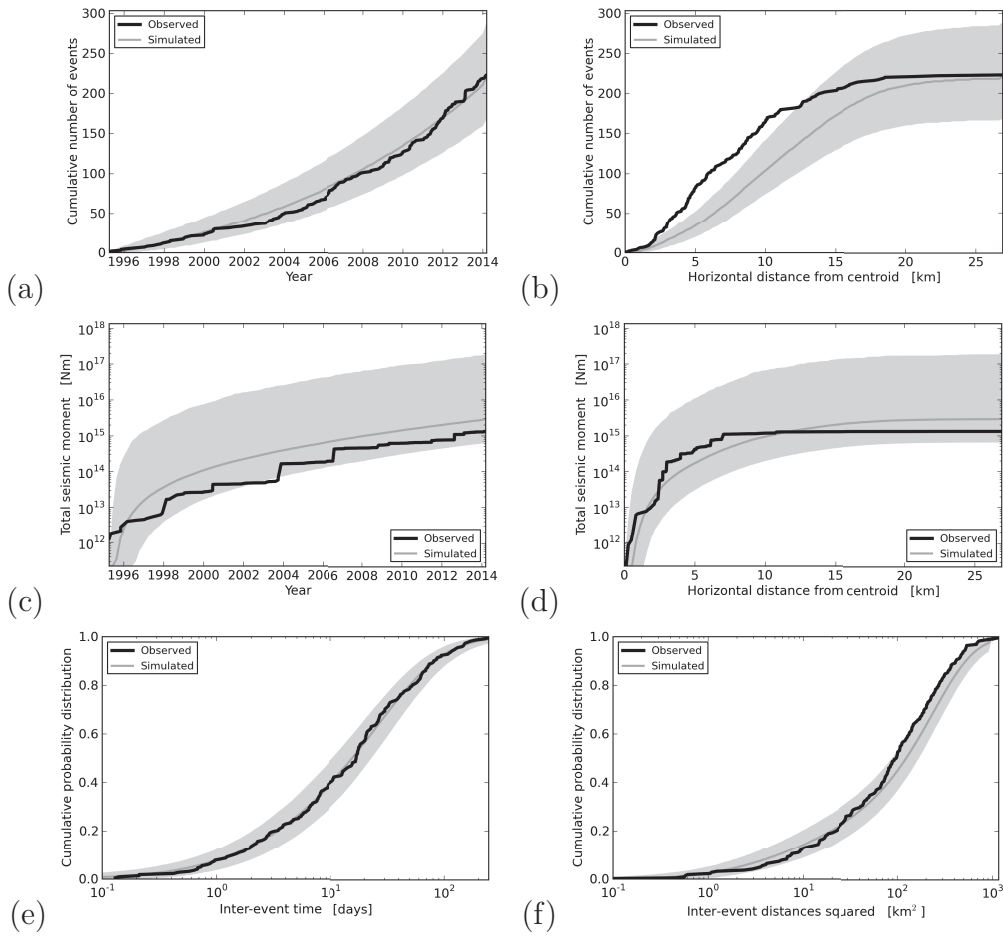


Figure 15: As Figure 9, except for the simulation results from the seismological model based on an exponential compaction trend Poisson process and an ETAS process. These simulations were based on Monte Carlo model parameter estimates. The dark grey line denotes the median simulation and the light grey band denotes the 95% confidence interval about the median.

from a Poisson distribution is expected as the events are no longer entirely independent of each other and some tendency towards event clustering will necessarily increase the variability in event numbers. The discrepancy in spatial localisation between the observed events and the median simulation remains unchanged but due to the increased variability, its statistical significance is slightly reduced to 3 ± 2 km (Figure 15b).

The slight systematic bias in total seismic moment remains as before, with the median simulation always exceeding the observed values from 1996 onwards. Again, as the bias does not appear to change with time (*i.e.* constant gap between the grey and black lines), one clear opportunity to reduce this bias is to investigate increasing the b -value slightly above its maximum likelihood estimate of $b = 1.0 \pm 0.2$ but still within its confidence interval.

4.2.1 Map variability

Figure 16 maps the observed and the median simulated event number density distributions and the differences between these two. Due to the relatively small number of events in the catalogue, there are considerable stochastic fluctuations in the event densities found in different simulated catalogues. From the confidence bound shown in Figure 15b it is apparent that 95% of this variability remains within $\pm 30\%$ of the median value. The largest event number densities found on these maps are 1 km^{-2} (observed) and

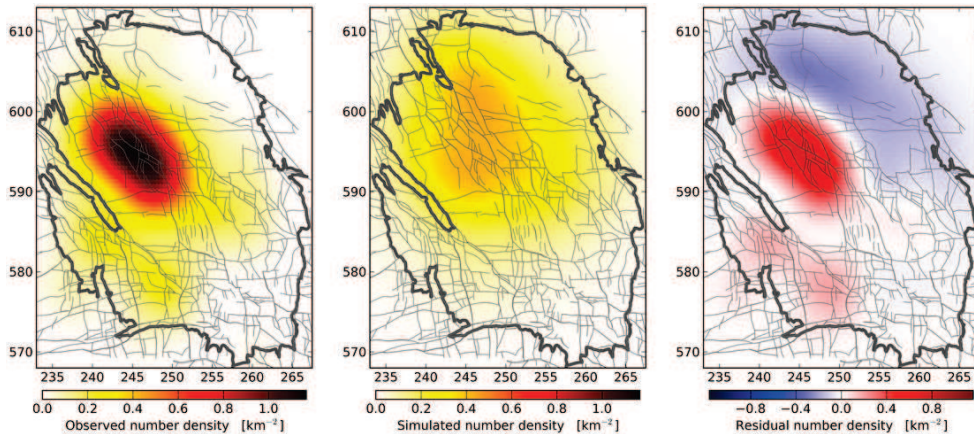


Figure 16: Maps of the observed and simulated number density and the residuals between them. Events densities were computed using the Gaussian kernel method. Simulation results were obtained using the full probability distribution of parameter estimates for the exponential compaction trend activity rates with epidemic type aftershock sequences.

$0.6 \pm 0.2 \text{ km}^2$ (median simulated \pm 95% confidence interval). This is a statistically significant difference and shows up as the largest red region in the residual map. However, as previously seen in Figure 15b this discrepancy is equivalent to a $3 \pm 2 \text{ km}$ shift in the simulated epicentres away from the centroid of observed epicentres.

There are two other regions of notable residuals. The largest is an area of negative residuals (blue) in a 10 km wide strip located just inside the field boundary and extending 25 km from the northern limit of the field to its eastern limit. The smallest is an area of positive residuals (red) located along the south-west field boundary. Both of these are also statistically significant although they relate to much smaller discrepancies.

We note the map of residuals between surface subsidence observed by geodetic levelling networks and computed from any of the existing compaction models (*pers. comm.* Biermann, 2014) shows a quite similar spatial pattern of residuals. These compaction models appear to systematically over-predict the observed subsidence along the north to north-east boundary of the field and under-predict subsidence along the south-west field boundary. This presents a clear opportunity to make a single update to these compaction models to improve the fit to historic subsidence and seismicity.

A further potential source of error in the existing compaction models is that they are possibly too smooth on length-scales less than 3 km. This is generally likely as surface subsidence is largely insensitive to variability in reservoir compaction on these length-scales because the 3 km thick overburden effectively filters this information out before it reaches the surface. This is a fundamental limit in the use of subsidence measurements to infer reservoir compaction as it takes an order of magnitude improvement in the signal-to-noise of subsidence measurements. However, we do recognise there may be other opportunities to improve the lateral resolution of reservoir compaction, such as using measurements of both horizontal and vertical surface displacements, or optimising the compaction model to simultaneously match the observed surface displacements and reservoir seismicity.

4.2.2 Annual variability

To better appreciate the year-to-year variability in the Acticity Rate model, Figure 17 shows how the annual event numbers and annual total seismic moments compare to this model between 1995 and 2014 and forecasts for future seismicity from 2014 to 2020 based on the current production plan. In both cases, the median simulation smoothly follows the trend of increasing annual seismicity with time, and the confidence bounds bracket the considerable year-to-year variability in observed seismicity. This is achieved without

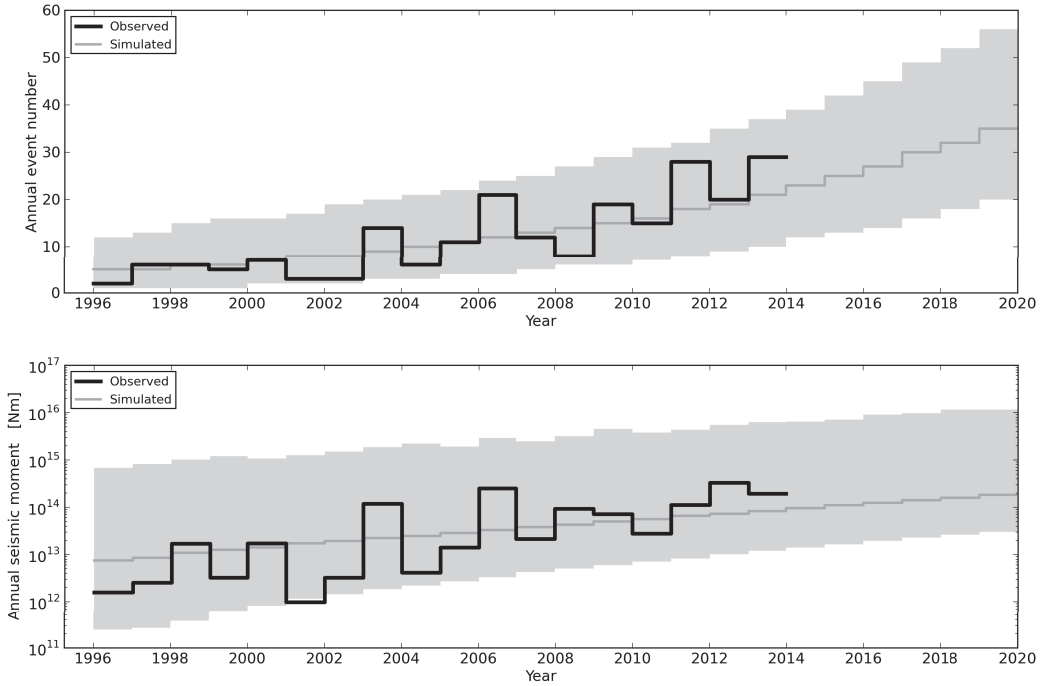


Figure 17: Annual number of $M \geq 1.5$ events, and the annual total seismic moment based on simulations of the Activity Rate model with aftershocks from 1996 to 2020 as compared to the observed seismicity from 1996 to 2014. The dark grey line denotes the median simulation and the light grey band denotes the 95% confidence interval about the median.

excessive large uncertainty bounds. The one slight and transient exception is due to the total seismic moment observed in 2001 just outside the lower confidence bound. This likely reflects the systematic bias in the model causing a tendency towards slight over prediction, which as stated before might be fixed by a slight increase in the b -value used for simulating event magnitudes.

4.2.3 Strain partitioning and b -values

As an additional check, we note the Activity Rate model also reproduces the observed exponential trend in strain partitioning with compaction (Figure 18a). Strain partitioning is measured as the fraction of reservoir strain accommodated by seismogenic fault slip and so depends on the total seismic moment per unit reservoir volume change. The Activity Rate model was not calibrated on this trend but independently reproduces it. This happens be-

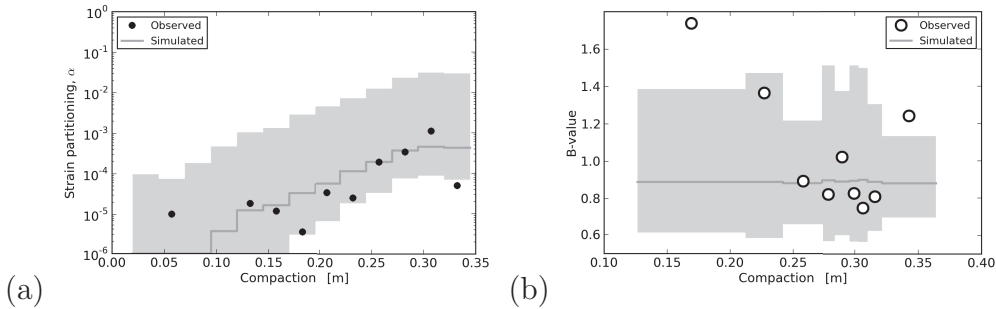


Figure 18: (a) Strain partitioning and (b) maximum likelihood estimates of b -value as functions of reservoir compaction. Observed seismicity is from April 1995 to August 2014. Simulations are based on the activity rate model with aftershocks shown in Figure 15. The dark grey line denotes the median simulation and the light grey band denotes the 95% confidence interval about the median.

cause event numbers per unit reservoir volume change increase exponentially with compaction and more events means more chance of a larger magnitude event and hence a larger total seismic moment.

Finally, we note the constant b -value assumed by seismological model is reproduced by the simulations and the apparent trend of decreasing b -value with increase compaction is hard to substantiate (Figure 18b). This is due to larger uncertainties in the estimated b -values that are inherent with the small sample size ($N = 50$) that must be used in any attempt at present to discern a trend with compaction.

4.2.4 Sensitivity to aftershock productivity

Recall that estimation of the ETAS a -value was largely uncertain due to the current limited range of magnitudes observed (Figure 13, top right). To investigate the influence of this epistemic uncertainty about the magnitude dependence of aftershock productivity, we ran additional simulations for $a = 0$ and $a = 1.8$ whilst all other parameters were fixed to their maximum likelihood estimates. Figure 19 shows that the median model remains a good fit to the observed number of events through time. The most notable difference is the much larger upper 95% confidence bound for $a = 1.8$. This makes sense for the following reason. For $a = 0$, event numbers do not depend on previous event magnitudes and the simulated event numbers are most like a Poisson distribution. For larger a -values the total number of events depends on previous event magnitudes that follow a Pareto distribution with its heavy tail above the median. Consequently, the ETAS a -parameter acts to propa-

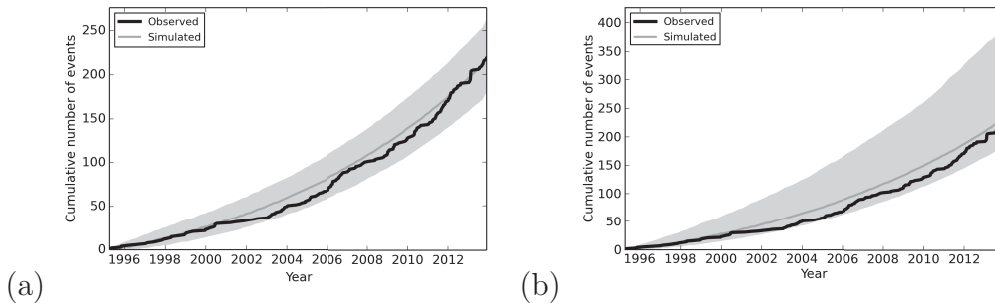


Figure 19: The estimated confidence interval for event numbers depends on the ETAS a parameter: (a) $a = 0$, (b) $a = 1.8$. Larger a -values means a larger upper bound to the confidence interval due to the larger number of aftershocks associated with larger magnitude events. Confidence bounds for $a > 0$ become increasing asymmetric about the median due to this coupling with event magnitudes that follow a Pareto frequency distribution. The dark grey line denotes the median simulation and the light grey band denotes the 95% confidence interval about the median.

gate the Pareto magnitude distribution into the event number distribution. This makes the ETAS a -parameter a clear target for reducing epistemic uncertainty about future seismicity and in particular obtaining a reliable upper bound to activity rate forecasts such as shown in Figure 17.

5 Do earthquakes cluster on mapped faults?

An earthquake typically involves slip on a fault which, more likely than not, will exploit and pre-existing fault as a surface of least resistance to slip. However, our knowledge of both earthquakes and faults within the Groningen Field is limited. Due to the current sparse nature of the earthquake monitoring network, earthquake depths are essentially unknown and their epicentres are uncertainty to within a standard random measurement error of 500 m (*pers. comm.* Doost, 2013). Due to typical resolution limits of the seismic reflection image pre-existing faults with throws less than 15 m cannot be reliably identified and mapped. Despite the considerable variability in maximum fault throw to fault length ratio (*e.g.* Kim and Sanderson, 2005), the typical value of 10^{-2} suggests faults shorter than 1500 m will be too small to map. A 1500 m long fault would be too small to reliably map but may still be large enough to host a magnitude 5 earthquake with a 10 MPa stress drop (Bourne and Oates, 2013, Table 2).

Although it is appealing to speculate about earthquakes clustering on

mapped faults - this need not be the case. Indeed, all the observed earthquakes, in principle, could have occurred on pre-existing faults that are too small to be mapped. The only way to decide is to compare the distribution of earthquake epicentres and mapped faults to test the hypothesis that earthquakes possess some tendency to preferentially cluster around mapped faults.

To begin, let us first consider which fault segments might be associated with most earthquakes. One simple way to do this is to move each earthquake onto the closest mapped fault segment and then count the number and seismic moment density along these fault segments (Figure 20). This reveals that every mapped fault within the general vicinity of the earthquakes is highlighted. There is no evidence that faults of any particular strike experience preferential seismicity. This makes sense that the uncertainty in epicentres is similar to the faults spacing (Figure 3).

Next, let us look in more detail at the distribution of offset distances between epicentres and the closest mapped fault to see if there is any weak evidence for earthquakes clustering closer to mapped faults rather than appearing with equal likelihood anywhere between mapped faults. The results of this analysis are shown in Figure 21. This reveals that $M \geq 1.5$ events exhibit a slight but statistically significant bias towards mapped faults when compared to stochastic simulations conditioned on the compaction but with no knowledge of the mapped faults themselves. This shows that half of the earthquakes are observed within 200 m of a mapped fault whereas for the simulated earthquakes this distance is 300 ± 50 m. This suggests the observed earthquakes are located at least 100 m closer to mapped faults than would be expected on the basis of pure chance. When we repeat this analysis for $M \geq 2, 2.5, 3$ there is a similar discrepancy but due to the smaller number of events available the confidence interval on the simulations are larger enough to explain these differences according to chance alone. As $M < 3.5$ earthquakes make no significant contribution to the seismic hazard Bourne et al. (2013) or risk the current evidence for clustering of $M < 2.5$ events around mapped faults does not need to be included in the seismological model.

Looking at this issue from another direction, we also tested the possibility that every observed event actually originated on a mapped fault but was miss-located due to the 500 m standard random error in epicentre determination. These two effects were included in the seismological model by simulating events as before, then relocating them on the closest mapped fault, and then relocating a second time by measurement error that was sampled from an isotropic bi-variant Gaussian distribution with a standard deviation of 500 m. This procedure happens to yield an excellent match with the observed distribution of epicentre to mapped fault distances for all magnitude

thresholds (Figure 22).

All these results mean that the current distribution of earthquakes could have originated from the distribution of mapped faults but we lack the precision to confidently reject the alternative hypothesis that mapped faults do not influence earthquake locations, at least those large enough to influence the seismic hazard and risk assessment. The upgraded earthquake monitoring network will provide a better opportunity to decisively resolve this issue. However, if all earthquakes are discovered to occur on mapped faults this is still unlikely to materially affect the seismic hazard and risk because it will typically require moving the simulated earthquake epicentres by only 300 m which will have little influence on the resulting ground motion distributions 3 km above the reservoir.

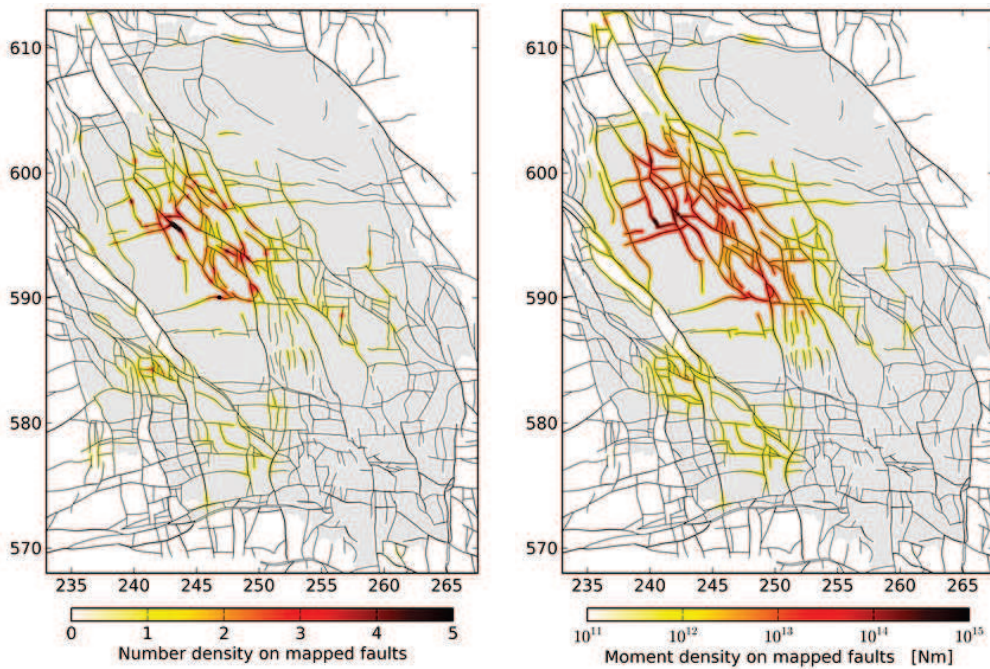


Figure 20: Estimates for the event number density (left) and the seismic moment density (right) obtained from the $M \geq 1.5$ events observed between April 1995 and December 2013 conditional on every event originating on a mapped fault.

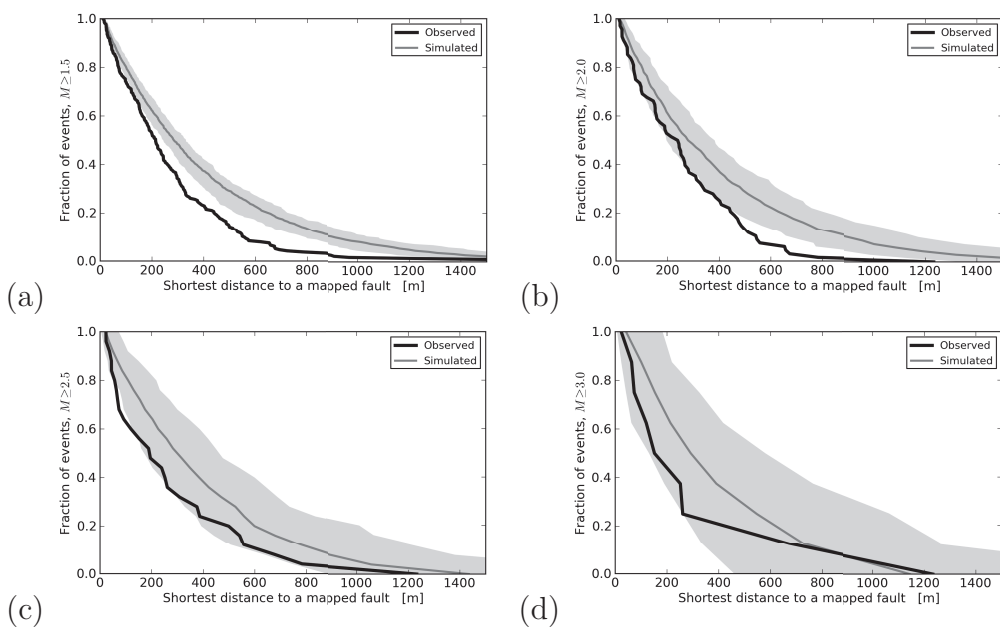


Figure 21: The fraction of epicentres located within a given distance of a mapped fault for all events of at least magnitude (a) 1.5, (b) 2.0, (c) 2.5, and (d) 3.0. For comparison, simulation results are shown as the median and 95% confidence interval according to the strain partitioning model with no clustering on mapped faults.

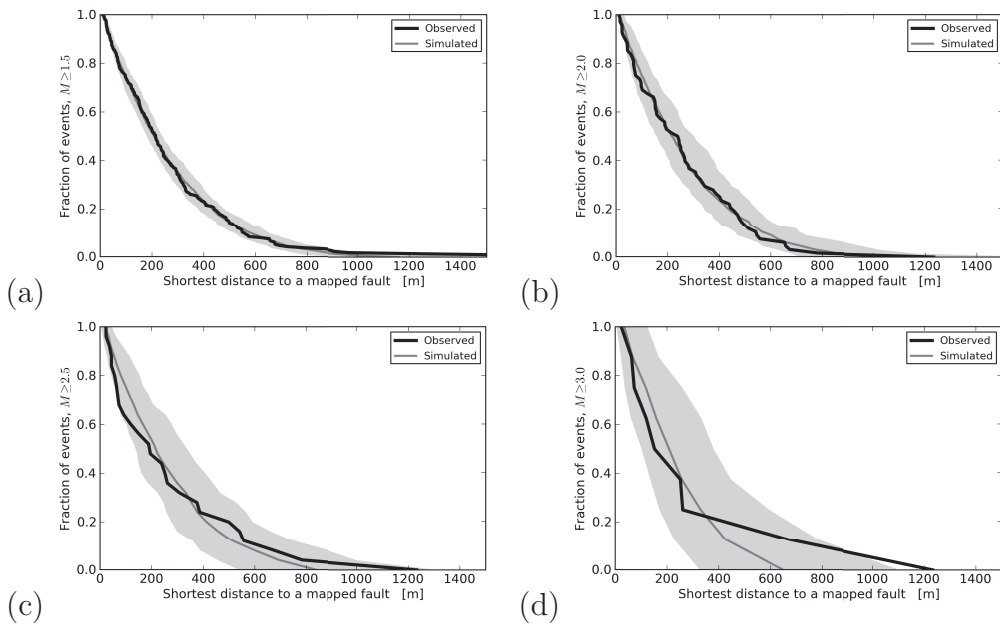


Figure 22: As Figure 21, except the simulations include clustering on mapped faults with a standard epicentral location error of 500 m.

6 Conclusions

Between 1960 and 2014 more than $2000 \times 10^9 \text{ m}^{-3}$ of hydrocarbon gas has been produced from the Groningen Field. This has induced a more-or-less uniform reservoir pressure depletion exceeding 25 MPa, a maximum surface subsidence of at least 350 mm, and more than 235 $M_L \geq 1.5$ earthquakes with a historic maximum of $M_L = 3.6$ in August 2012. The induced seismicity is a cause of considerable concern due to the possibility of future earthquake ground motions causing damage to buildings and also possibly injury to the occupants.

Probabilistic seismic risk assessment is a well-established method for characterising the size of this risk as well as its geographical extent and distribution across different building typologies. If necessary, options to mitigate this seismic risk include reservoir pressure maintenance, regulating future gas production rates, retro-fitting selected existing buildings to improve their structural resilience and ensuring new buildings are designed for earthquake resilience.

A necessary part of probabilistic risk assessment is a seismological model that provides a means of forecasting the probability distribution of future earthquakes in terms of their numbers, locations, magnitudes, and focal mechanisms. The first seismological model developed for the Groningen Field was the Strain Partitioning model (Bourne and Oates, 2013; Bourne et al., 2014b). To assess and potentially reduce epistemic uncertainties in this model, an alternative model has been developed - the Activity Rate model. Both models exploit the observed conformance between historical subsidence and seismicity. The geomechanical basis for this is that the induced earthquakes play a role in accommodating the induced deformations within and around the reservoir due to reservoir compaction.

There are two key measures of seismicity in relation to this deformation, the total seismic moment per unit reservoir volume decrease and the total number of events per unit reservoir volume decrease. Both measures exhibit clear exponential-like trends with reservoir compaction. The Activity Rate model succeeds in representing this trend more precisely than the Strain Partitioning model. Moreover it benefits from more reliable parameter estimates using formal maximum likelihood methods and also avoids the need for expert judgement as the data do not need to be arranged in bins. This contrasts with the Strain Partitioning model that uses an approximation to the Pareto sum distribution and requires a choice of bin size to estimate parameters linking seismicity to compaction.

The evidence for aftershocks within the historic earthquake catalogue is not obvious with casual inspection due to the small number of observed

events, but simulation-based analysis reveals statistically significant evidence for their presence. Furthermore, the temporal, spatial and magnitude trigger effects may be quantified in accordance with the Epidemic Type Aftershock Sequence model. Joint maximum likelihood estimation of the compaction and aftershock model parameters leads to an Activity Rate model that matches almost all aspects of the observed seismicity.

Two minor exceptions offer opportunities for further improvement to the Activity Rate model. First, the model has a slight tendency to over-predict the total seismic moments. This will likely be resolved by including the frequency-magnitude b -value parameter in the joint maximum likelihood estimation scheme. Second, the model has a slight tendency to under-predict the spatial localisation of event numbers (≤ 3 km) within the region of greatest compaction and seismicity. This will likely be resolved by updating the reservoir compaction model to improve its fit to geodetic observations of surface displacements as well as quantification of uncertainty in the estimated values of the compaction model parameters.

7 Recommendations for further work

We identify the following opportunities for further improvements to the seismological model:

- Investigate updating the existing compaction models to improve the fit to geodetic measurements of surface displacements and to improve the performance of the seismological model.
- Quantify the influence of compaction uncertainty on the seismological model and incorporate these uncertainties into the existing work flow for Probabilistic Seismic Hazard and Risk Assessment.
- Investigate the utility of alternative functional forms for the relationship between the rate of event nucleation and the rate of reservoir compaction such as an inverse power-law.
- Investigate the possibility of b -value decreasing with compaction, or otherwise revising the b -value to avoid the slight tendency to over-predict seismic moments. Also assess the sensitivity to uncertainty in b -value, possibly through including b -value in the joint parameter estimation process.
- Investigate the use of Bayesian inference (using MCMC) as a more computationally efficient alternative to the current maximum likelihood Monte Carlo approach for parameter estimation and stochastic simulation.

Acknowledgements

We are grateful to Onno van der Wal, Anthony Mossop, Rob van Eijs, Stijn Bierman, and Famke Kraaijeveld for informative discussions about the reservoir compaction model. Philip Jonathan helped to guide our ideas about statistical modelling, and Julian Bommer, Helen Crowley and Rui Pinho provided us with an expert introduction to contemporary methods in Probabilistic Seismic Hazard and Risk Assessment. We thank Jan van Elk and Dirk Doornhof for their continuing encouragement and support. The implementation of the Activity Rate model made use of SciPy (Eric Jones et al., 2001) and most of the figures were created using Matplotlib (Hunter, 2007). Finally, we benefited from careful reviews of this work by Philip Jonathan and Christopher Harris; although any errors that still remain are our own.

References

- Aki, K., 1965. Maximum likelihood estimation of b in the formula $\log N = a - bM$ and its confidence limits. *Bulletin of the Earthquake Research Institute of Tokyo University* 43, 237–239.
- Bourne, S.J., Oates, S., 2012. Probability of an earthquake greater than magnitude 4 due to gas production from the Groningen Field. Technical Report. Shell Global Solutions International. Rijswijk, The Netherlands.
- Bourne, S.J., Oates, S., 2013. Induced strain and induced earthquakes within the Groningen Gas Field: Earthquake probability estimates associated with future gas production. Technical Report. Shell Global Solutions International. Rijswijk, The Netherlands.
- Bourne, S.J., Oates, S.J., Bommer, J.J., 2013. A probabilistic seismic hazard assessment for the Groningen Field. Technical Report. Nederlandse Aardolie Maatschappij B.V.. Assen, The Netherlands.
- Bourne, S.J., Oates, S.J., Bommer, J.J., Dost, B., van Elk, J., Doornhof, D., 2014a. A Monte Carlo method for probabilistic hazard assessment of induced seismicity due to conventional natural gas production. Submitted to *Bull. Seis. Soc. Am.* .
- Bourne, S.J., Oates, S.J., van Elk, J., Doornhof, D., 2014b. A seismological model for earthquakes induced by fluid extraction from a subsurface reservoir. Submitted to *J Geophys Res Solid Earth* .
- Cornell, C., 1968. Engineering seismic risk analysis. *Bull. Seismol. Soc. Am.* 58, 1503–1606.
- Davison, A., 2003. *Statistical models*. Cambridge University Press.
- Eric Jones, Oliphant, T., Peterson, P., Others, 2001. SciPy: Open source scientific tools for Python. <http://www.scipy.org/>.
- Gutenberg, B., Richter, C., 1954. *Seismicity of the Earth and Associated Phenomena*. Princeton University Press, Princeton, New Jersey. 2nd edition.
- Hanks, T., Kanamori, H., 1979. Moment magnitude scale. *Journal of Geophysical Research* 84, 2348–2350.
- Hunter, J.D., 2007. Matplotlib: A 2D graphics environment. *Computing In Science & Engineering* 9, 90–95.

- Kim, Y.S., Sanderson, D.J., 2005. The relationship between displacement and length of faults: A review. *Earth-Science Reviews* 68, 317–334.
- Kostrov, V.V., 1974. Seismic moment and energy of earthquakes, and seismic flow of rocks. *Izv. Acad. Sci. USSR Phys. Solid Earth*, 1, Eng. Transl. , 23–44.
- Marzocchi, W., Sandri, L., 2003. A review and new insights on the estimation of the b-value and its uncertainty. *Annals of Geophysics* 46, 1271–1282.
- McGarr, A., 1976. Seismic Moments and Volume Changes. *Journal of Geophysical Research* 81, 1487–1494.
- McGuire, R., 2008. Probabilistic seismic hazard analysis: Early history. *Earthquake Engineering & Structural Dynamics* 37, 329–338.
- Mena, B., Wiemer, S., Bachmann, C., 2013. Building robust models to forecast induced seismicity related to geothermal reservoir enhancement. *Bulletin of the Seismological Society of America* 103, 383–393.
- Nelder, J., Mead, R., 1965. A simplex method for function minimization. *The Computer Journal* 7, 308–313.
- Ogata, Y., 1998. Space-time point-process models for earthquake occurrences. *Ann. Inst. Statist. Math.* 50, 379–402.
- Ogata, Y., 2011. Significant improvements of the space-time ETAS model for forecasting of accurate baseline seismicity. *Earth, Planets and Space* 63, 217–229.
- Schoenberg, F.P., 2013. Facilitated Estimation of ETAS. *Bulletin of the Seismological Society of America* 103, 601–605.
- Scott, D., 1992. *Multivariate Density Estimation: Theory, Practice, and Visualization*. John Wiley & Sons, Ltd, New York, Chicester.
- Shapiro, S., Dinske, C., Langenbruch, C., 2010. Seismogenic index and magnitude probability of earthquakes. *The Leading Edge March*.
- Shapiro, S.a., Krüger, O.S., Dinske, C., 2013. Probability of inducing given-magnitude earthquakes by perturbing finite volumes of rocks. *Journal of Geophysical Research: Solid Earth* 118, 3557–3575.
- Utsu, T., 1966. A statistical significance test of the difference in b-value between two earthquake groups. *Journal of Physics of The Earth* 14, 37–40.

Appendices

A The strain-partitioning model

For comparison with the activity rate model, Figures 23 and 24 show the performance of the strain-partitioning model over the period of historic seismicity from April 1995 to August 2014. These are quite similar in terms of temporal and spatial distribution of total seismic moments. The median event numbers are also similarly distributed. However, the most notable difference is that the upper bound of the 95% confidence interval for event numbers is significantly larger. This reflects the strong dependence on the Pareto sum distribution as event numbers are determined by the modelling requirement to achieve a certain total seismic moment. This could be interpreted as a member of the activity rate model where the ETAS a -parameter becomes large.

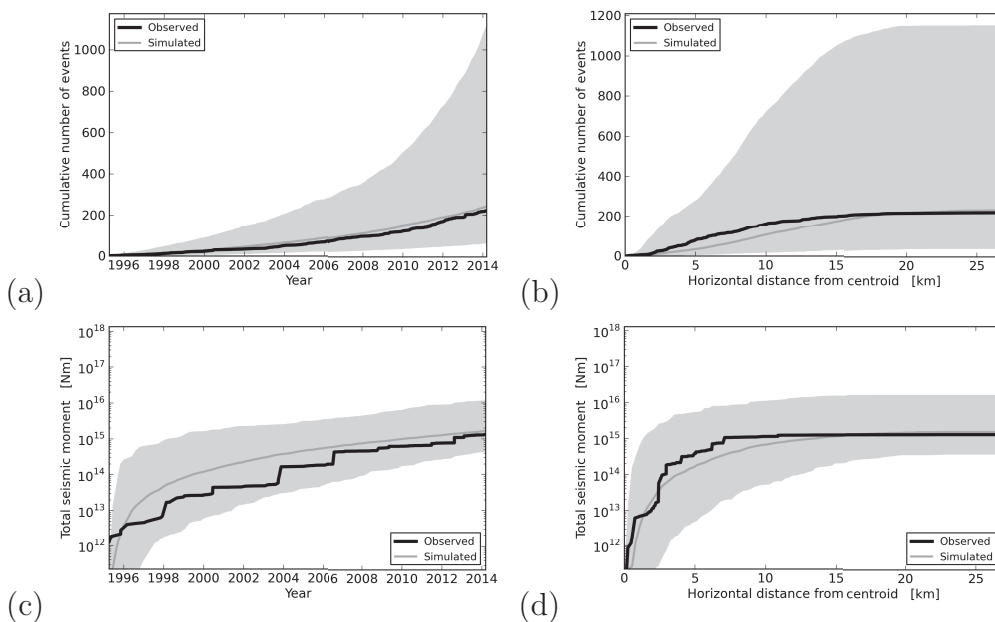


Figure 23: Comparison of simulated and observed data for the strain partitioning model.

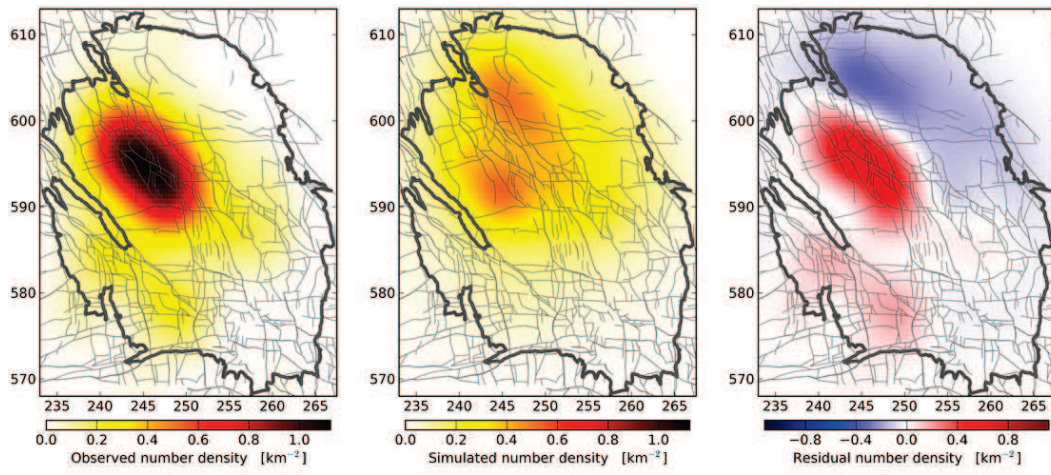


Figure 24: As Figure 16, except for the strain partitioning model.